Tuning Interface Dynamics of Benzene-Based Molecular Dipoles for High Capacity and Long Lifespan in Lithium Metal Batteries

Chae Yeong Son, Daehyun Kim, Huiju Kim, Haesun Park,* and Won-Hee Ryu*

Lithium metal batteries (LMBs), which possess the lowest reduction potential and exceptional capacity, have long been regarded as the ultimate solution for realizing ultrahigh energy storage systems. However, dendritic Li formation poses significant challenges, leading to performance degradation and safety hazards. This study emphasizes the importance of controlling the functional edge structures of benzene-derived molecular electrolyte additives to achieve rapid and long-term LMB performance, thereby proposing benzoate sodium salt (BZ-COO) as a promising candidate. Finally, Li-Li symmetric cells employing BZ—COO exhibit exceptional cycling performance over 1600 cycles even under harsh conditions (5 mA cm^{-2}), outperforming benzene additives with —CH$_3$ or —CHO substituents. This study provides a novel perspective on the development of surface flattening electrolyte additives for rapid operation and extended lifespan of LMBs.

1. Introduction

As a cornerstone of energy storage technology, lithium-ion batteries (LIB) continue to advance, driving their application across diverse fields and increasing demand for superior performance.[1] With growing emphasis on longevity, safety, and efficiency in energy storage, lithium metal batteries (LMBs) that employ Li metal as the anode are emerging as promising candidates for next-generation battery technologies.[2] The Li metal anode is regarded as the ultimate anode owing to its lowest redox potential (-3.04 V vs SHE), high theoretical capacity (3860 mAh g^{-1}), and

C. Y. Son, H. Kim, W.-H. Ryu
Department of Chemical and Biological Engineering
Sookmyung Women's University
100 Cheongpa-ro 47-gil, Yongsan-gu, Seoul 04310, Republic of Korea
E-mail: whryu@sookmyung.ac.kr
D. Kim, H. Park
School of Integrative Engineering
Chung-Ang University
84 Heukseok-ro, Dongjak-gu, Seoul 06974, Republic of Korea
E-mail: parkh@cau.ac.kr
W.-H. Ryu
Institute of Advanced Materials and Systems
Sookmyung Women's University
100 Cheongpa-ro 47-gil, Yongsan-gu, Seoul 04310, Republic of Korea

low gravimetric density (0.534 g cm^{-3}).[3] Unfortunately, the high reactivity of Li significantly hinders its practical application and commercialization, limiting its potential to replace LIBs.[4] During repeated charge–discharge cycles, localized Li nucleation occurs at the defect sites on Li metal, and subsequent nucleation and growth are accelerated at the nodular Li tips, leading to the rapid formation of fractal-like Li structures called Li dendrites.[5] Whisker-like dendrites arise from inherent (electro-)chemical instability at the interface between Li metal and the electrolyte.[6] As the elongated Li structures grow, they can penetrate the separator, potentially causing thermal runaway and catastrophic safety failures such as explosions.[7] Meanwhile, mossy metallic Li grows in a tip-growing morphology owing to electrolyte transport limitations.[8] This moss-like dendritic Li yields substantial amounts of dead Li that detach during Li stripping, drastically reducing the coulombic efficiency (CE).[9] Dendrites also induce capacity loss, increase interfacial resistance, and trigger side reactions, resulting in overall performance degradation.[10] In addition, unprotected Li actively reacts with organic electrolytes, resulting in an unstable solid–electrolyte interphase (SEI) layer, additional dead Li formation, severe volumetric expansion, and electrolyte depletion.[11] Addressing the fatal dendrite formation and interface side reactions is critical for ensuring the safety and long lifespan of LMBs.

A variety of strategies have been explored to mitigate dendritic Li growth in LMBs. Rational host design, interfacial chemistry regulation, and electrolyte optimization have all been developed to promote compact, uniform lithium deposition.[12] Among these strategies, advancing electrolytes with functional additives is an effective way to directly stabilize lithium metal anodes.[13] The electrolyte, which forms an interface with the Li electrode, plays a critical role in the performance of the anode by facilitating the migration of dissociated Li ions and interacting closely with the Li surface.[14] Electrolyte additives have been designed to simultaneously perform multiple functions, such as surface flattening, durable SEI layer formation, and reversible Li deposition/dissolution.[15] However, precise control of the additive molecular structure and a deeper understanding of their mechanisms are required to develop economically viable, high-performance LMBs.
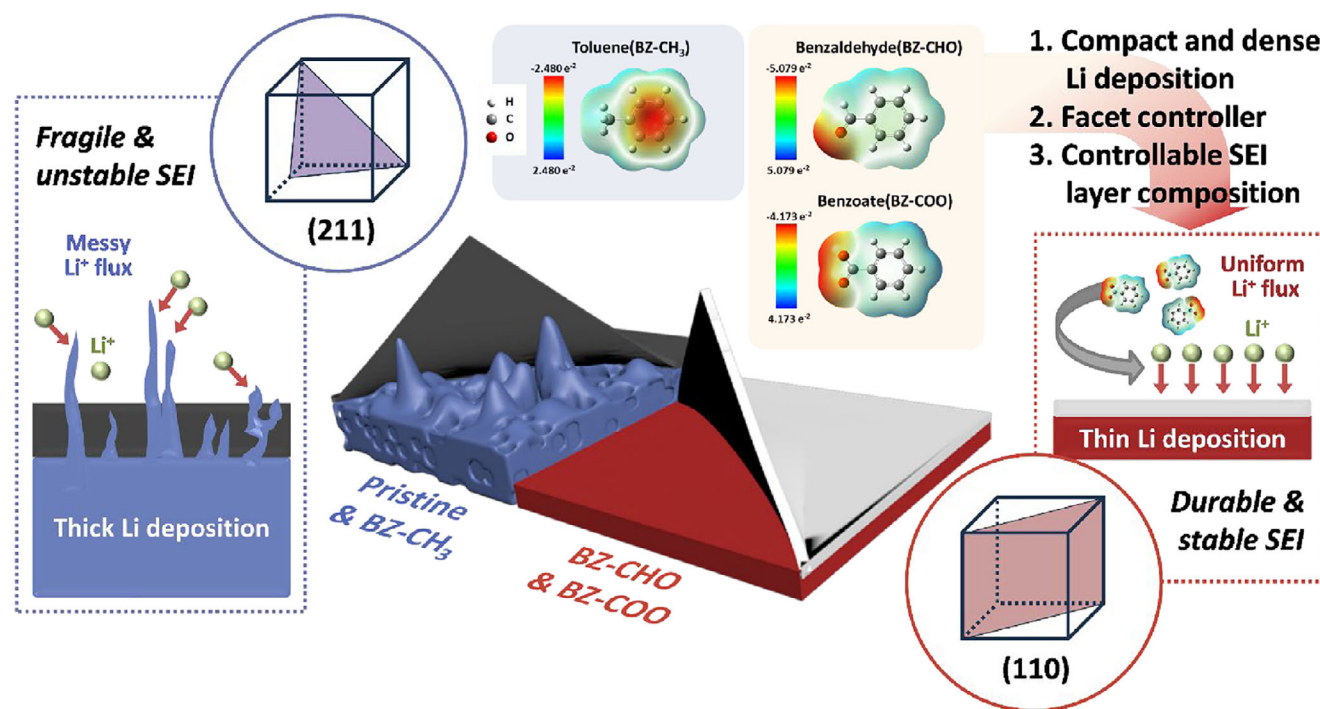
Figure 1. Schematic of Li deposition behavior influenced by benzene-based additives with different functional groups (BZ-CH$_3$, BZ-CHO, and BZ-COO).

In this study, we manipulated the structural motifs of dipolar benzene molecules using carbon-based functional groups as electrolyte additives to develop high capacity and long cycle LMBs. We investigated the impact of oxygen-containing functional groups on Li deposition by comparing toluene (BZ-CH$_3$), benzaldehyde (BZ-CHO), and benzoate (BZ-COO), in which the hydrogen atoms in benzene were replaced by —CH$_3$, —CHO, and –COO groups, respectively (**Figure 1**). This comparison aims to understand how the chemical structure of benzene-based electrolyte additives, particularly changes in substituents, influences the homogeneity and efficiency of lithium deposition. We observed the morphologies and roughness factors of the Li metal after cycling with different functionalized benzene additives. The charge transfer behavior and energy levels of the molecules were examined to understand the interfacial interaction features. The interface composition after the SEI formation process was also elucidated using 3-D depth profiles obtained by time-of-flight secondary ion mass spectrometry (TOF-SIMS) to confirm the structural and chemical characteristics of the modified SEI layers. We also utilized density functional theory (DFT) to calculate the binding energies between each additive on Li and predict the preferred orientation of the molecular dipole additives. Electrochemical tests were conducted using Li-Li symmetric cells at various current densities and capacity limits to demonstrate the cycling performance of the benzene-based molecular additives. By modulating the functional groups of molecular dipole additives, we provide an effective solution to suppress root- and tip-growing fractal-like dendrites, minimize side reactions, and thereby extend LMB cycle life.

2. Results and Discussion

2.1. Morphological Characterization from Li-Li Symmetric Cells

Uniform lithium deposition and stripping during charge–discharge cycles are crucial for long-term cycling stability in LIBs. An uneven electrode surface causes a localized current concentration at the nodular spot on the interface between the electrolyte and the electrode, inducing irregular Li nucleation and consequent dendritic lithium growth.[16] The dendritic Li deposition significantly impairs the lifespan of LMBs and triggers numerous undesirable side reactions. Therefore, smoothing of the electrode surface is essential for long-term battery operation. Here, we introduce surface-flattening and interface-restructuring electrolyte additives employing benzene-based molecules with different functional groups (-CH$_3$, -CHO, and -COO). To verify the effects on the surface roughness of the Li metal anode, morphological analysis was performed using ex situ scanning electron microscopy (SEM). Li metal was collected from Li-Li symmetric cells cycled for 50 and 500 cycles at a current density of 5 mA cm^{-2} with a capacity limit of 1 mAh cm^{-2} (**Figure 2a–f**; Figure S1, Supporting Information). After 50 cycles, the surface morphology of the Li metal cycled without additives exhibited a series of mossy dendrites and byproducts in grooved regions. (Figure 2a; Figure S1a, Supporting Information). With BZ-CH$_3$, distinct whisker-like protrusions covered much of the amorphous surfaces (Figure 2b; Figure S1b, Supporting Information). The local nucleation and subsequent formation of elongated whisker-shaped Li deposits are formed on the defect sites of the Li metal due to the accumulated compressive mechanical stress beneath the SEI layer.[17]
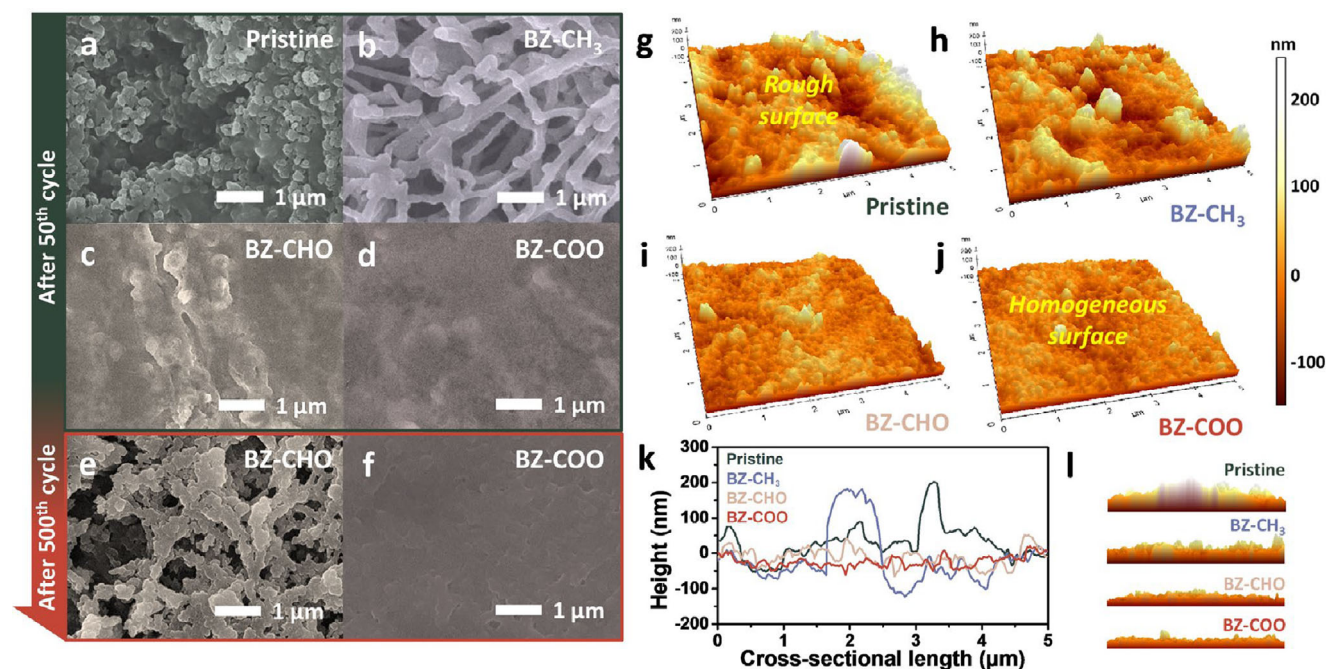
ADVANCED
SCIENCE NEWS
www.advancedsciencenews.com

NANO · MICRO
small
www.small-journal.com

Figure 2. SEM images of Li–Li symmetric cells cycled at 5 mA cm^{-2} and 1 mAh cm^{-2} a–d) for 50 cycles and e,f) 500 cycles without additives and with BZ-CH$_3$, BZ-CHO, or BZ-COO. g–j) AFM 3D topography of Li electrodes after 100 cycles at 5 mA cm^{-2} and 0.5 mAh cm^{-2}. k) Height–length profiles and l) vertical AFM cross-sections for each condition.

Conversely, the Li metal anodes with BZ-CHO and BZ-COO displayed smoother surfaces without the distinct appearance of dendrites or pits (Figure 2c,d; Figure S1c,d, Supporting Information). Additionally, the Li metal electrodes cycled after 500 cycles were analyzed to compare the leveling effects of functionalized benzene-based additives during long-term cycling. In the cases without additives and with BZ-CH$_3$, unwanted short circuits and cell failure were observed before 500 cycles. The Li anodes in the electrolyte containing BZ-CHO were covered with numerous intertwined Li wires and undesirable side-reaction products after 500 cycles (Figure 2e; Figure S1e, Supporting Information). This indicates that BZ-CHO is insufficient to prevent rapid electrolyte consumption during long term operation, as the extensive fibrous Li structure leads to premature failure under continuous charge–discharge cycling. In contrast, Li electrodes with BZ-COO consistently maintained the flattest, densest surface characteristics over extended cycles compared to other additives (Figure 2f; Figure S1f, Supporting Information). Visual inspection of Li metal surfaces disassembled from the Li-Li symmetric cells after 50 cycles (Figure S2, Supporting Information) showed that both the pristine and BZ-CH$_3$-incorporating electrodes exhibited extensive black regions, indicative of reaction byproducts such as dead Li (Figure S2a,b, Supporting Information). In contrast, the appearance of the lithium metals prepared with BZ-CHO and BZ-COO was similar to that of a fresh lithium electrode, exhibiting a silver-like shine (Figure S2c,d, Supporting Information). This observation directly verified that the Li anodes maintained smooth surfaces during plating and stripping. However, after 500 cycles, the electrode containing BZ-CHO was predominantly covered in darkened regions with little metallic sheen, unlike the Li metal electrode with BZ-COO, which main-

tained a shiny surface. The SEM results clearly demonstrate the impact of BZ-COO on the morphological characteristics of Li deposition, highlighting its potential to mitigate dendritic growth and undesirable byproduct generation despite prolonged cycling.

To assess the roughness and height of the electrode surface, atomic force microscopy (AFM) measurements at the microscopic scale were conducted with Li metals cycled 100 times at 5 mA cm^{-2} and 0.5 mAh cm^{-2}, as shown in Figure 2g–l and Figure S3 (Supporting Information). 3D topography images enabled detailed analysis of surface texture and possible structural anomalies, such as Li dendrites. Pristine and BZ-CH$_3$-cycled electrodes exhibited rough surfaces, indicating the irregular surface growth and stripping behavior of Li. In contrast, both Li metal anodes cycled with BZ-CHO and BZ-COO maintained flat surfaces without whisker-like Li growth even after 100 cycles. Figure 2k highlights height profiles across the surface section. For a more quantitative comparison, the results numerically indicated that BZ-COO has the lowest R$_a$ (R$_q$) roughness values (20.2 nm (25.7 nm)) among the other Li metal electrodes (44.3 nm (57.5 nm)) for the Li electrode without additive, 37.1 nm (37.9 nm) with BZ-CH$_3$, 21.2 nm (27.8 nm) with BZ-CHO (Figure S3, Supporting Information). Furthermore, in Figure 2l, the vertical images show the thickness of the Li metal. Owing to the incompact Li plating, both the pristine and BZ-CH$_3$-containing Li electrodes exhibited much thicker Li metals with obvious height fluctuations. Porous structures exhibit macroscopic transport limitations. Conversely, the height uniformity was significantly higher in the Li metals prepared in the electrolytes with BZ-CHO and BZ-COO than in the other Li electrodes. Therefore, the Li electrodes cycled with BZ-CHO and BZ-COO exhibited dense and nonporous lithium deposits. In the case of the Li anodes with

ADVANCED
SCIENCE NEWS

www.advancedsciencenews.com

NANO · MICRO
small
www.small-journal.com

BZ-COO, the morphological properties exhibited the flattest and thinnest deposition without protrusion tips. The results suggest that the smoothest surface was observed with BZ-COO, indicating its superior effectiveness in promoting uniform and dense lithium deposition compared to the other additives and the pristine condition. These results demonstrate that controlling the functional group, even on the same benzene molecule backbone, is a critical determinant of the electrolyte additive for achieving a flattened surface of the Li metal anode for long cycles.

2.2. SEI layer composition of Li metal after 100 cycles

The SEI layer inevitably forms through Li-corrosion reactions and (electro-)chemical decomposition of electrolyte species.[18] The beneficial formation of a durable SEI layer over dozens of cycles is essential for stabilizing and protecting the Li electrode interface against further side reactions and volume changes. During Li plating, severe volumetric expansion occurs, causing stress to accumulate beneath the SEI. This stress leads to cracks at weaker sites in the SEI layer.[19] Such cracks relieve compressive stress but extrude lithium, resulting in unnecessary electrolyte consumption and additional side reactions. To sustain a uniform, crack-free electrode surface and stable Li-metal kinetics during continuous cycling, the SEI layer must possess high ionic conductivity and mechanical robustness.

To understand the decomposition behavior of electrolyte species, including the additives, we calculated the highest occupied molecular orbital (HOMO) and lowest unoccupied molecular orbital (LUMO) energies of the tetraethylene glycol dimethyl ether (TEGDME) solvent, and of the BZ-CH$_3$, BZ-CHO, and BZ-COO additives with GaussView (Figure S4, Supporting Information). A lower LUMO energy level indicates a tendency for preferential reduction of the functionalized benzene molecules, serving as an indicator of how strongly an additive contributes to SEI formation on the anode surface.

DFT calculations were performed to examine electron transfer behavior between each additive and the Li metal surface. Using Bader charge analysis (**Figure 3**a), we assessed how many electrons each additive extracts from the Li surface. For additives absorbed on the Li metal surface, electron transfer from the Li surface to the additive represents the reduction tendency. As illustrated in Figure 3b, BZ-CHO and BZ-COO extract more than two electrons without additional electrons, whereas BZ-CH$_3$ extracts only a limited amount (BZ-CH$_3$, 0.48e; BZ-CHO, 2.23e; and BZ-COO, 2.83e). When two additional electrons are present in the Li surface model with each additive, BZ-COO still shows a stronger propensity for electron extraction from the Li metal than BZ-CH$_3$ and BZ-CHO (BZ-CH$_3$: 0.90e, BZ-CHO: 2.58e, and BZ-COO: 3.17e). These calculations suggest that the strong electron affinity of BZ-COO facilitates the reduction of additives during SEI film formation.

To investigate the SEI component and surface nature after cycling, we conducted X-ray photoelectron spectroscopy (XPS) on Li metal cycled 100 times at a current density of 5 mA cm^{-2} with a limit capacity of 0.5 mAh cm^{-2} (Figure S5, Supporting Information). Electrolyte-derived by-products such as C—H, C—O, and —CF$_3$ were observed on all electrolytes—-pristine and those with BZ-CH$_3$, BZ-CHO, and BZ—COO—-reflecting SEI forma-

tion. Nanoscale XPS analysis did not reveal distinct changes in the surface composition, likely because repeated cycling constantly modifies the surface. To conduct a broader comparison at the microscale, time-of-flight secondary ion mass spectroscopy (TOF-SIMS) was utilized with Li electrodes disassembled from the Li-Li cells under identical conditions (Figure 3b–g; Figure S6, Supporting Information). The SEI layer consists of inorganic–organic mixtures. Inorganic components such as LiF and Li$_2$CO$_3$, which are protective and durable, are crucial for extending the lifespan of LMBs.[20] Compared with the Li anodes lacking additives or containing BZ-CH$_3$, the LiF signals were broader and more abundant in the Li electrodes cycled with BZ-CHO and BZ-COO (Figure 3c). The portion of the CO$_3^-$ component in the Li metal anode decreased in both Li electrodes without additives and with BZ-CH$_3$ (Figure 3d). Conversely, the sustained CO$_3^-$ content along the deeper regions of the Li metal cycled with BZ-CHO and BZ-COO indicated higher and deeper levels of mobilizable carbonate components within the SEI layer. The LiF component has high mechanical strength with a wide bandgap, and the Li$_2$CO$_3$ component has low hygroscopicity and high ionic conductivity.[21] While Li$_2$CO$_3$ alone has a small bandgap and low surface energy that lead to SEI dissolution, the coexistence of LiF and Li$_2$CO$_3$ species offers synergistic advantages: reduced electron tunneling and maintained ionic mobility, thereby suppressing dendrite growth.[22] The cycled Li electrode with BZ-COO exhibited the highest ratio of LiF and Li$_2$CO$_3$ signals, indicating the formation of a highly conductive and robust SEI layer. Similarly, Figure S6a (Supporting Information) shows that CN$^-$ species cover the deepest region of the Li electrode cycled with BZ-COO. Li$_2$O content remained similar for all samples, suggesting it arises from general electrolyte decomposition (Figure 3e). In contrast to the Li anodes without additives and with BZ-CH$_3$ and BZ-CHO, which exhibited low signals in the few deeper regions, suggesting porous deposition, a higher proportion of Li$^-$ species and a compact structure were detected even in the deep region for Li metals cycled with BZ-COO (Figure 3f). For a clearer understanding, the TOF-SIMS results are summarized using intensity sputter time profiles, which provide a more detailed view of the SEI composition at different depths (Figure 3g,h; Figure S6b–c, Supporting Information). The cycled Li electrodes utilizing BZ-COO exhibited the highest levels of CO$_3^{2-}$, LiF, and Li$^-$ signals across the entire metal, compared to all other). Ultimately, it was verified that the introduction of BZ-COO reconstructed the SEI layer characteristics with high Li$^+$ diffusivity and enhanced durability.

2.3. Crystallinity of deposited Lithium after 10 cycles and DFT calculation

Examining the crystalline structure of cycled lithium metal is crucial for determining whether lithium deposition occurs homogeneously and planarly or grows dendritically. Ex situ XRD analysis was performed on Li metal extracted from Li-Li cells cycled at a 1 mA cm^{-2} with 1 mAh cm^{-2} for 10 cycles. As shown in Figure S7 (Supporting Information), the unreacted lithium metal before cycling exhibits typical and distinct (200) and (110) peaks. After cycling without additives, the Li anodes showed a higher intensity of the (200) peak and a negligibly reduced (110) peak
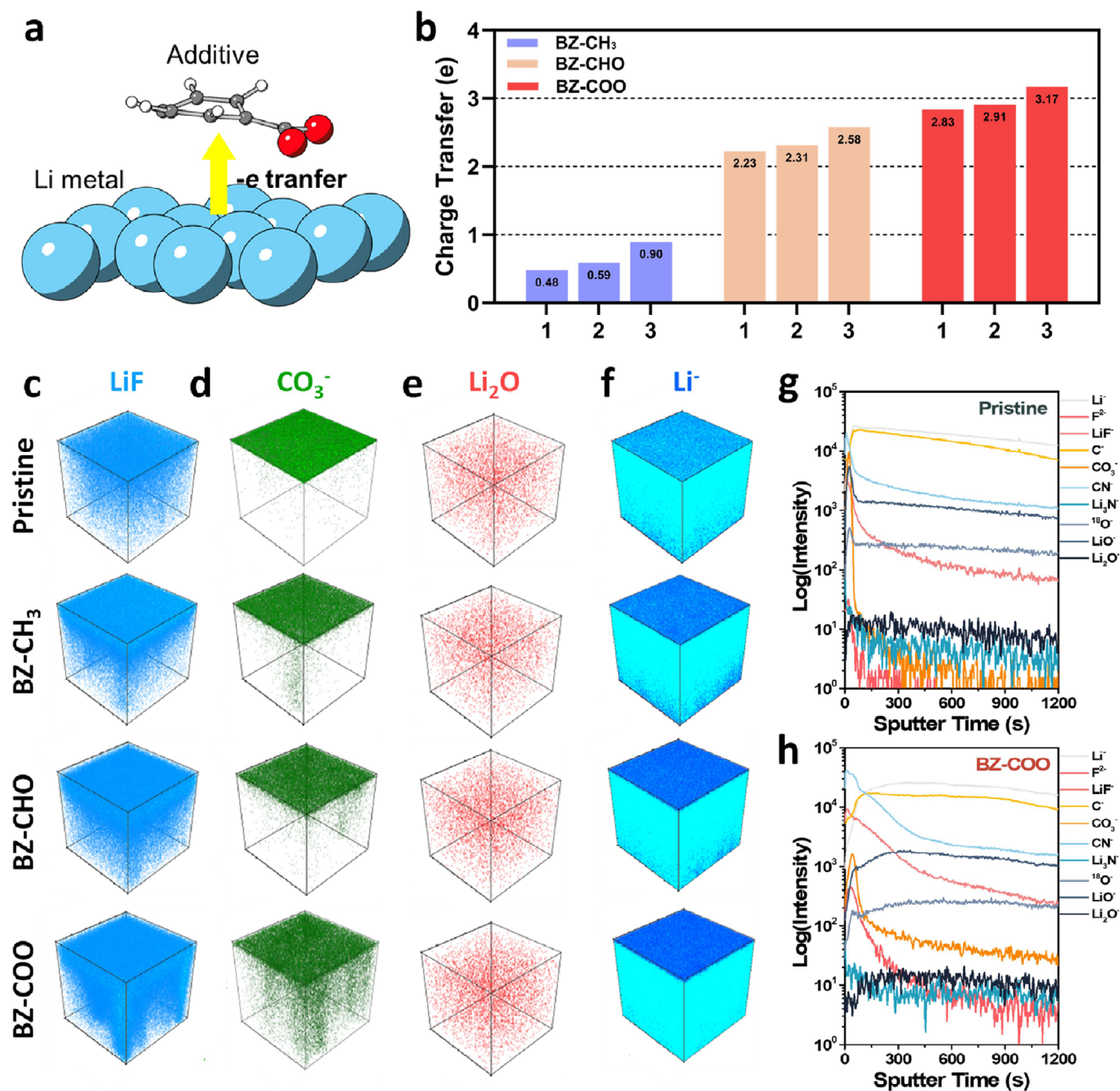
**ADVANCED
SCIENCE NEWS**

www.advancedsciencenews.com

NANO · MICRO

small

www.small-journal.com

Figure 3. SEI layer properties of the Li-metal electrode in the Li-Li symmetric cells after 100 cycles. a) Schematic of electron transfer from the Li metal surface to the additive. b) Quantitative electron transfer from the Li metal surface to each additive with and without additional electrons in the surface. c–f) TOF-SIMS 3D depth profiles along sputter time from the Li metals without and with different benzene-based additives (BZ-CH$_3$, BZ-CHO, and BZ-COO): c) LiF, d) CO$_3^-$, e) Li$_2$O, and f) Li$^-$ signal. g–h) Log(intensity)-sputter time profiles of Li metals comparing pristine and BZ-COO electrodes.

(**Figure** 4a). A larger portion of the (110) surface is related to the flattening of the Li surface. Based on the thermodynamic computational results, the establishment of the lowest migration energy barrier of the (110) lattice enabled a dendrite-free planar morphology with low porosity.[23] With BZ-CH$_3$ and BZ-CHO, the Li electrodes displayed relatively similar intensities of (110), (200), and (211) peaks, resembling the structural features of fresh Li metal. These results suggest that the additives BZ-CH$_3$ and BZ-CHO do not significantly influence the crystal phase of the de-

posited lithium during cycling, indicating that their role is more focused on affecting the plating behavior. However, the obvious (110) peak was higher than the (200) peaks for the Li anodes with BZ-COO, which ensured the ability to effectively suppress the Li whiskers of BZ-COO. To better understand the suppression capabilities of the additives, the results are summarized as ratios in Figure 4b. BZ-COO showed an overwhelmingly high (110) plane value of 87% compared to all other samples (13% without additives, 24% for BZ-CH$_3$, and 23% for BZ-CHO). Figure 4b shows

ADVANCED
SCIENCE NEWS

www.advancedsciencenews.com

NANO · MICRO
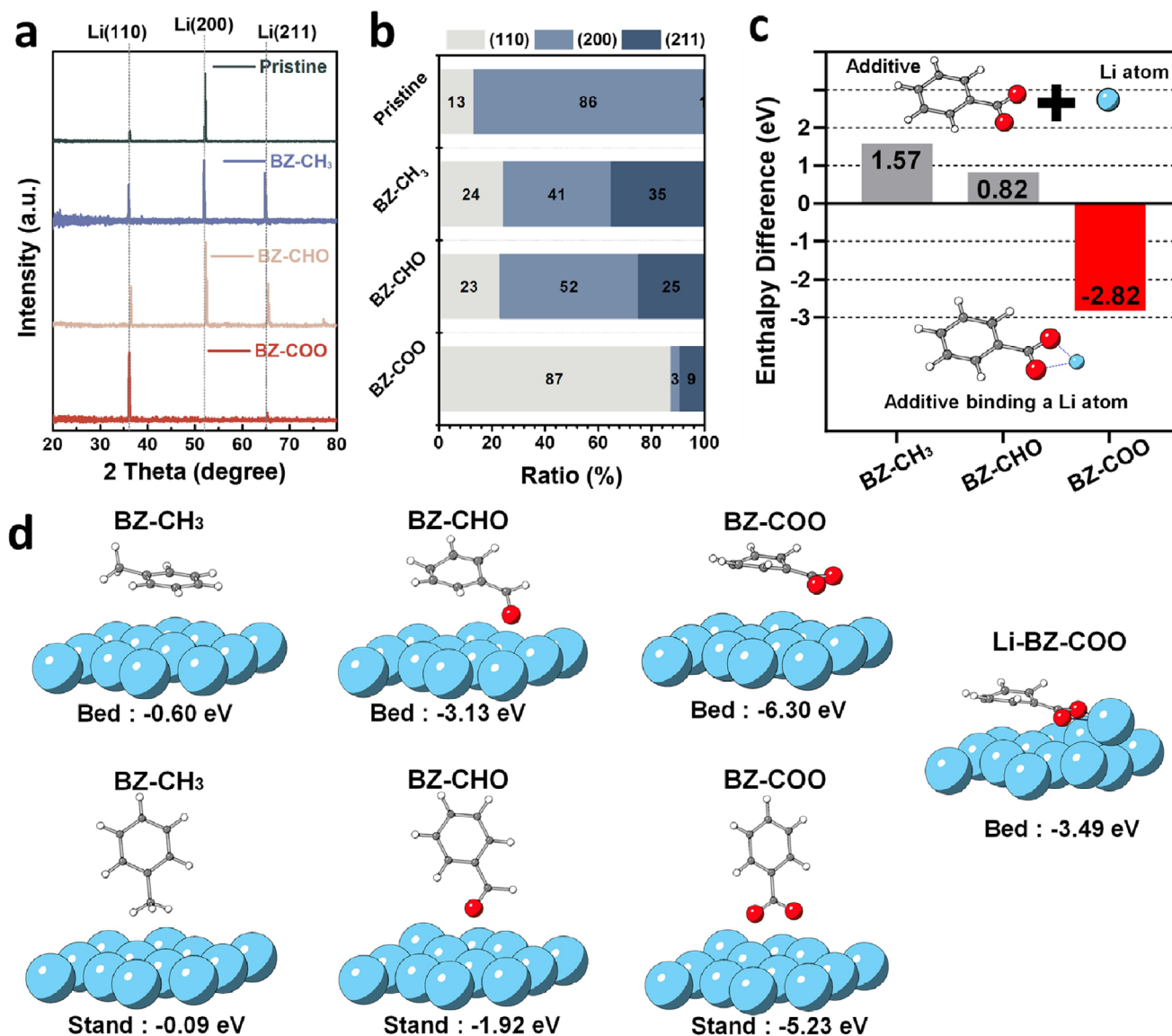**small**
www.small-journal.com

Figure 4. Crystalline characterization of Li electrodes after 10 cycles: a) XRD analysis conducted from the Li-Li symmetric cells, and b) The ratio graph of the XRD data. c) Enthalpy difference of additives between remaining separated from Li atom and binding a Li atom (Enthalpy difference = $E_{\text{additive binding with a Li atom}} - E_{\text{additive}} - E_{\text{Li atom}}$). d) adsorption energy of each additive on the Li metal surface. The "Bed" orientation refers to the additive being horizontal, allowing the entire atoms to interact with the Li surface, while the vertical "Stand" orientation indicates that selected atoms are in direct biding with the surface.

that BZ-COO strongly influenced the crystallographic rearrangement of Li metal, which continuously reacted throughout the cycling process.

To evaluate the effect of the additive on the Li plating behavior, we examined whether each additive interacted with the Li atoms within the electrolyte. Based on binding energy calculations (Figure 4c), BZ-CH$_3$ and BZ-CHO predominantly remained separate from Li atoms, whereas BZ-COO exhibited a tendency to bond with the Li atoms. The low affinity of an additive for Li atoms diminishes its regulatory effect on Li deposition during the charging process. Consequently, we infer that the high affinity of BZ-COO for Li atoms enhances its impact on Li deposition compared to those of BZ-CH$_3$ and BZ-CHO.

To further investigate the interaction between the additive and the Li metal surface, we compared the adsorption behaviors of BZ-CH$_3$, BZ-CHO, and BZ-COO on the Li metal surface. As illustrated in Figure 4d, we considered two different additive orientations on the Li surface: the Bed and Stand orientations. The "Bed" orientation refers to the additive being horizontal, allowing the entire atoms to interact with the Li surface, while the vertical "Stand" orientation indicates that selected atoms are in direct binding with the surface. BZ-COO exhibits the strongest adsorption energy in both orientations of the additives compared to BZ-CH$_3$ and BZ-CHO (BZ-COO Bed: −6.30 eV and Stand: −5.23 eV). BZ-CH$_3$, which has the weakest binding affinity with a Li atom, also shows the weakest binding on the Li surface

ADVANCED
SCIENCE NEWS

www.advancedsciencenews.com

NANO · MICRO
small
www.small-journal.com

(BZ-CH$_3$ Bed: −0.60 eV and Stand: −0.09 eV). This indicates that the adsorption of BZ-CH$_3$ onto the Li metal surface is likely less favorable than that of BZ-CHO and BZ-COO, resulting in a reduced capacity to modulate the overall Li plating dynamics.

To investigate the interaction between the additive bonded to a Li atom and the anode surface, we evaluated the adsorption energy of BZ-COO complexed with a Li atom (Li-BZ-COO) on a Li metal surface. Li-BZ-COO exhibited reduced binding affinity to the Li metal surface compared to that of BZ-COO. Nevertheless, it retained a stronger adsorption tendency than BZ-CH$_3$ and BZ-CHO in the "Bed" orientation (BZ-CH$_3$: -0.60 eV, BZ-CHO: -3.13 eV, and Li-BZ-COO: -3.49 eV). This suggests that, even when solvated with a Li atom, the additive has a significant influence on the anode surface. To further examine the reduction behavior of Li-BZ-COO, we performed Bader charge analysis, which revealed that Li-BZ-COO retains a strong propensity for extracting electrons from the Li metal surface (Figure S8, Supporting Information). These calculations indicate that, among the considered additives, BZ-COO is the most susceptible to reduction at the Li metal surface, leading to subsequent SEI formation.

2.4. Electrochemical Stability of Li-Li Symmetric Cells Including BZ-CH$_3$, BZ-CHO, and BZ-COO

For the optimal concentration, we evaluated the cycling stability of Li–Li symmetric cells with varying amounts of BZ-COO (Figure S9, Supporting Information). Electrolytes containing 0.1, 0.5, and 1 wt.% (almost saturation) of BZ-COO were tested under a current density of 5 mA cm^{-2} and an areal capacity of 1 mAh cm^{-2}. Among the tested concentrations, the 1 wt.% BZ-COO electrolyte enabled the most prolonged and stable cell operation. Based on these results, all subsequent electrochemical measurements in this study were conducted using 1 wt.% BZ-COO. To investigate the resistance of the interfacial layer, electrochemical impedance spectroscopy (EIS) was performed using Li-Li symmetric cells incorporating different electrolyte additives with symmetric circuits (**Figure 5**a–c; Figure S10, Supporting Information). The solution resistance (R$_{sol}$) and charge-transfer resistance (R$_{ct}$) profoundly influence the electrochemical kinetics of the anode; their values reflect the characteristics of the electrode interface under notorious conditions, such as the presence of additives.[24] Therefore, the R$_{ct}$ value is useful for understanding interfacial reactions during charging and discharging.[25] Before cycling, all Li-Li cells exhibited similar impedance values of ≈350 Ω, with negligible differences among them (Figure 5a). However, definite differences emerged after the electrochemical reactions during cycling, as shown in Figure 5b. After the 20th cycle, the Li-Li cells without additives and those with BZ-CH$_3$ displayed R$_{ct}$ values of 55.75 and 87.81 Ω, respectively, significantly higher than those of cells employing BZ-CHO (33.15 Ω) and BZ-COO (28.78 Ω). In pristine and BZ-CH$_3$-containing cells, the R$_{ct}$ values increased sharply after 40 and 60 cycles, displaying apparently higher resistance compared to both cells prepared with BZ-CHO and BZ-COO. During repeated Li deposition and dissolution, fractal-like protrusion tips increased the electrode surface area, while the detachment of Li dendrite stripping reduced the surface active area. Because R$_{ct}$ is inversely proportional to the charge-transfer active area, the higher impedance after 40 cy-

cles compared to after 60 cycles can be attributed to the significant amount of Li dendrite growth. The results align with the dipole moment and polarizability order presented in Figure S11 (Supporting Information), as represented in the resistance cycle number profiles (Figure 5c). The additive with the highest dipole moment and polarizability demonstrates the most pronounced interaction with the Li metal anode under a strong electric field. Such enhanced dipolar characteristics facilitate more effective adsorption onto the Li surface, thereby reinforcing interfacial stabilization and improving the long term cycling stability. Conversely, the cells employing BZ-COO consistently maintained stable and lower resistance values throughout the cycling, indicating that introducing BZ-COO produced a highly stable Li/electrolyte interface and facilitated efficient charge transfer.

Li-Li symmetric cell tests were conducted at various current densities and capacities to demonstrate the surface stabilization effects of the additives through long-term lifespan characteristics under severe operating conditions (Figure 5d–g; Figures S12 and S13, Supporting Information). Under a low current density of 1 mA cm^{-2} with capacities of 1 and 3 mAh cm^{-2}, the Li-Li cells without additives showed rapid voltage increases (Figure 5d,e). These cells reached 0.5 V at 208 and 192 h, respectively, indicating severe interfacial degradation of the Li anode. Similar sudden voltage spikes at 73 and 97 h were observed in cells containing BZ-CH$_3$, which exhibited overvoltages of ≈110 and ≈180 mV, and an even faster short-circuit than the pristine cells (Figures S12a–d, and S13a,b, Supporting Information). The results suggest that BZ-CH$_3$ does not function effectively as a stabilizing agent; instead, it impedes electrolyte performance and causes operational difficulties. In contrast, cells with BZ-CHO showed stable cycling performance, maintaining a voltage of ≈100 mV over an extended period (≈600 h) at 1 mAh cm^{-2} (Figure S13a,b, Supporting Information). However, at a high capacity of 3 mAh cm^{-2}, serious overpotential fluctuations appeared after 400 h (Figure S12c,d, Supporting Information) and, while BZ-CHO effectively reduced interfacial resistance and enhanced cell performance, its effects were not sustainable over long lifespans at higher capacities. This degradation in cycling stability is attributed to the formation of dendrites and inactive Li accumulation during cycling, which leads to SEI reformation and other side reactions that hinder Li-ion transport. The acceleration of these unwanted reactions over extended cycling diminishes the effectiveness of the surface planarizer. In contrast, Li symmetric cells with BZ-COO molecular additives afforded exceptional cycling stability, operating for over 1000 h and 900 h under low and high capacity conditions, respectively. Notably, BZ-COO cells maintained a significantly lower average voltage of 55 mV with minimal fluctuations, indicating that BZ-COO contributed significantly to the stabilization of the Li metal anode surface, even after 450 cycles at 1 mAh cm^{-2}. Similar results were obtained at high current densities. At high current densities, Li ions accumulate more easily at tip and defect sites on the electrode surface, promoting the rapid growth of whisker-like entangled Li and challenging long-term operation. As shown in Figure 5f and Figures S12e and S13c (Supporting Information), both Li-Li cells without additives and those with BZ-CH$_3$ displayed a rapid voltage increase within 100 h, indicating a low Li stabilization capability. Although cells containing BZ-CHO maintained ≈160 mV for over 246 h, the overpotential rose steadily, surpassing 0.5 V at ≈350 h (Figure S12f, Supporting
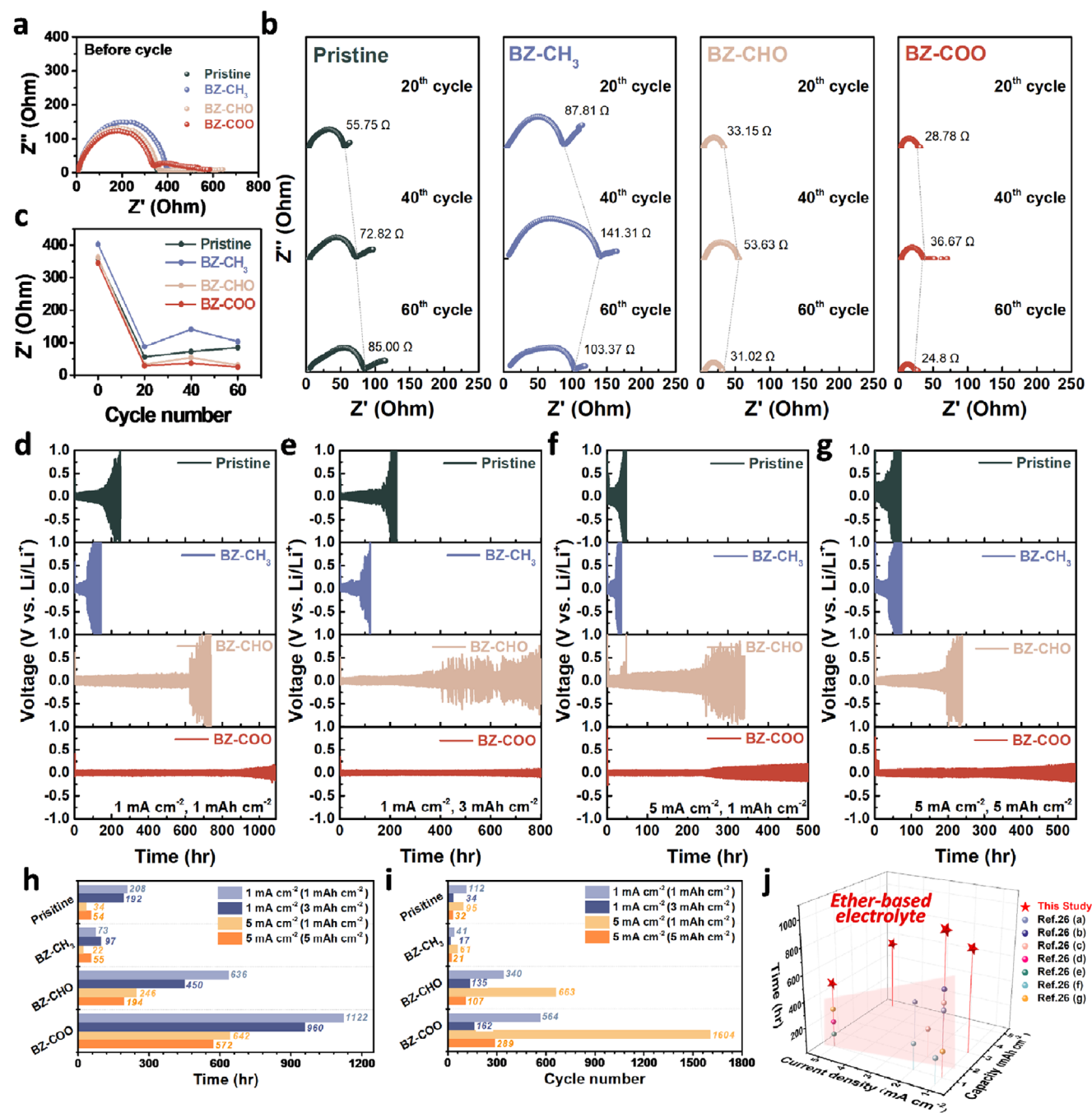
Figure 5. Electrochemical performance of Li-Li symmetric cells in the absence and presence of BZ-CH$_3$, BZ-CHO, and BZ-COO under various conditions. a–c) EIS spectra: a) before cycling, b) after the 20th, 40th, and 60th cycles, c) resistance value with respect to the cycle number. d–j) Li-Li symmetric cells cycled under low current density of 1 mA cm^{-2}: with a capacity of (d) 1 mAh cm^{-2} and (e) 3 mAh cm^{-2}, and f–g) under a high current density of 5 mA cm^{-2}: with a capacity of (f) 1 mAh cm^{-2} and (g) 5 mAh cm^{-2}. h) Time and i) cycle-number comparison for Li-Li symmetric cells without and with additives (BZ-CH$_3$, BZ-CHO, and BZ-COO). j) Comparative graph of cycling stability for Li-Li symmetric cells using ether-based electrolytes under diverse current densities and capacities.

Information). However, in the case of cells containing BZ-COO, the voltage began to increase slightly from 333 h but then stabilized with only minor oscillations, maintaining excellent stability for up to 1600 cycles. The results demonstrated that BZ-COO significantly enhanced the stabilization of the Li surface, even at a high current density. Additionally, we carried out the Li-Li symmetric cell test with very harsh conditions of high current density (5 mA cm^{-2}) and high capacity (5 mAh cm^{-2}). Both Li-Li cells without additives and those with BZ-CH$_3$ exhibited a rapid voltage increase with a large overpotential within 70 h (Figure 5g;

**ADVANCED
SCIENCE NEWS**

www.advancedsciencenews.com

**NANO · MICRO
small**

www.small-journal.com

Figures S12g and S13d, Supporting Information). In contrast, stable operation with a low average voltage of 120 mV was displayed in the Li-Li cells containing BZ-CHO, but a sharp voltage rise occurred at 194 h, indicating electrolyte depletion (Figure S12h, Supporting Information). Remarkably, exceptionally stable cycling was observed in the case of the presence of the BZ-COO additive, with 55 mV at 300 h and with 130 mV after 880 cycles.

To more clearly compare the cell test results, we plotted the time and cycle number required for each Li-Li symmetric cell to reach a voltage of 0.5 V, categorizing them by additive and test condition (Figure 5h,i). The results of the cell tests showed a similar tendency across all conditions, with the cells containing BZ-CHO and BZ-COO operating for extended periods and dozens of cycles, followed by cells without any additives, and finally those with BZ-CH$_3$. In particular, the cells prepared with BZ-COO exhibited an impressive cycle life of over 1600 cycles at 5 mA cm^{-2}, indicating that BZ-COO offers a notable advantage for stabilizing the Li metal surface. Furthermore, we reviewed previously reported studies on ether-based electrolytes and plotted the cell operation times under different conditions in a 3D graph, as shown in Figure 5j.[26] Although the cells were tested under various conditions in previous studies, we believe that the cells with optimized functionalized benzene-based molecular additives achieved excellent electrochemical performance. This study paves the way for the development of optimal electrolyte additives through molecular functional-group engineering, thereby enabling further breakthroughs in LMB technology.

3. Conclusion

In this study, we reported the functional group effects of benzene-based molecular dipole electrolyte additives on the surface reactions of Li metal anodes to achieve rapid operation and long-lifespan LMBs. We intentionally introduced three functional groups (-CH$_3$, -CHO, and -COO) by controlling the number of oxygen species in the benzene backbone. Among these additives, benzoate (BZ-COO) exhibited superior performance by effectively regulating Li nucleation and promoting uniform, planar Li surface deposition. Compared with other functionalized benzene derivatives, BZ-COO facilitated flattened (110) directional crystalline growth against dendritic growth along the (200) and (211) planes. In addition, the formation of a highly stable SEI layer with abundant LiF and Li$_2$;CO$_3$; components was enabled by the introduction of BZ-COO, which contributed to enhanced ionic conductivity and mechanical durability. The electrochemical evaluations confirmed that Li-Li symmetric cells incorporating BZ-COO maintained stable cycling performance under harsh operating conditions, including high current density (5 mA cm^{-2}) and large capacity limits (5 mAh cm^{-2}). In contrast, additives with -CH$_3$; and -CHO substituents displayed limited stabilizing effects, leading to the formation of whisker-like dendritic lithium and accelerated electrolyte depletion. Computational analysis further elucidated the adsorption behaviors and binding affinities of these additives, revealing that BZ-COO preferentially interacted with Li metal and reinforced planar, defect-free crystalline growth along the (110) facet. Overall, this study underscored the potential of molecular-dipole engineering as a promising strategy for optimizing electrolyte additives in LMBs. By finely tuning the functional groups of electrolyte additives, it

was possible to achieve significantly longer battery lifespans and higher energy efficiencies, thereby addressing critical challenges associated with Li metal anodes. These findings pave the way for the development of electrolyte-additive technology to realize future ready high energy storage systems with assured safety and durability.

4. Experimental Section

Materials and Chemicals: Tetraethylene glycol dimethyl ether (TEGDME, 99%) was employed as a solvent after dehydration using freshly activated 4 Å molecular sieves. Lithium bis(trifluoromethane)sulfonimide (LiTFSI, 99.95%) was added to the electrolyte. Toluene (BZ-CH$_3$), benzaldehyde (BZ-CHO), and sodium benzoate salt (BZ-COO) were used as the electrolyte additives. All the materials were sourced from Sigma–Aldrich (Korea).

Preparation of Li-Li Symmetric Cells: The Li-Li cell tests were performed using R2032 coin-type cells (Wellcos Corp.) assembled in an Ar-filled glove box. Each cell was composed of a lithium foil (12 mm in diameter) and a separator (Celgard 2500 polypropylene). The electrolyte contained 1 M LiTFSI dissolved in TEGDME with 1 wt.% of BZ-CH$_3$, BZ-CHO, or BZ-COO. A Li metal anode with a diameter of 12 mm was employed.

Electrochemical Measurements: Charge–discharge tests on Li-Li symmetric cells were performed using a battery cycler (WBCS3000S battery test system, WonATech). EIS measurements were performed from 1 MHz to 0.01 Hz at an amplitude of 5 mV.

Ex Situ Characterization: The crystal structures of the Li electrodes were analyzed using X-ray diffraction (XRD; D8 Advance, Bruker) with a Cu-Kα source ($\lambda = 1.54$ Å). The surface morphologies of the Li metal electrodes were examined by field-emission scanning electron microscopy (FE-SEM; JSM-7600F, JEOL). The surface roughness of the samples was assessed by AFM (NX-10) in a glove box. The Li metal characteristics after cycling were explored using XPS (K-alpha, Thermo U.K.) and TOF-SIMS. TOF-SIMS was conducted using a TOF.SIMS5 instrument (ION-TOF, Münster, Germany) and negative-polarity data were collected using a 30 keV Bi^{3+} ion source. The area of analysis was 100 × 100 μm. Depth profiles were obtained by sputtering ion beams of Cs$^+$ (3 keV) on a 300 × 300 μm square. The sputtering rate was measured on Na metal as 0.6752 nm s^{-1} with a sputtered area of 300 × 300 μm

Computational Details: DFT calculations were performed using the Vienna ab initio simulation package (VASP) to investigate the impact of benzene-based electrolyte additives on Li plating behavior.[27] Projector-augmented wave potentials were used to describe the core contributions, and a plane-wave basis set was used for the valence electrons with a cut-off energy of 520 eV.[28] The Perdew–Burke–Ernzerhof generalized gradient approximation (GGA) of the exchange correlation functional was employed for correlation effects.[29] An Γ-point centered k-point mesh of 5 × 3 × 1 and an electronic convergence criterion of 10^{-5} eV were used for all calculations.

To model the additive on the Li metal surface, the (1 1 0) facet of the Li BCC structure was constructed with five layers, which have 10.32 Å in the *x*-direction and 14.59 Å in the *y*-direction, including a vacuum region of 24 Å in the *z*-direction.[30] For all

**ADVANCED
SCIENCE NEWS**

www.advancedsciencenews.com

**NANO · MICRO
small**

www.small-journal.com

calculations, the two bottom layers of the surface model were fixed to their bulk positions. The adsorption energies of the additives on the Li metal surface were calculated as follows:

$$\Delta E_{ads} = \Delta E_{surface+additive} - \Delta E_{surface} - \Delta E_{additive} \tag{1}$$

where $\Delta E_{surface + additive}$ is the total energy of the Li surface model with the additive, $\Delta E_{surface}$ is the total energy of the isolated Li metal surface, and $\Delta E_{additive}$ is the energy of the additive. The calculation cell was relaxed to an atomic-force tolerance of 0.05 eV Å^{-1}. In addition, a Bader charge analysis was performed to evaluate the charge of the additive absorbed on the surface.[31]

Supporting Information

Supporting Information is available from the Wiley Online Library or from the author.

Conflict of Interest

The authors declare no conflict of interest.

Data Availability Statement

The data that support the findings of this study are available from the corresponding author upon reasonable request.

[1] H. Kim, G. Jeong, Y.-U. Kim, J.-H. Kim, C.-M. Park, H.-J. Sohn, *Chem. Soc. Rev.* **2013**, *42*, 9011.

[2] a) D.-H. Liu, Z. Bai, M. Li, A. Yu, D. Luo, W. Liu, L. Yang, J. Lu, K. Amine, Z. Chen, *Chem. Soc. Rev.* **2020**, *49*, 5407; b) D. Lin, Y. Liu, Y. Cui, *Nat. Nanotechnol.* **2017**, *12*, 194.

[3] a) M. Wang, C. Jiang, S. Zhang, X. Song, Y. Tang, H.-M. Cheng, *Nat. Chem.* **2018**, *10*, 667; b) W. Xu, J. Wang, F. Ding, X. Chen, E. Nasybulin, Y. Zhang, J.-G. Zhang, *Energy Environ. Sci.* **2014**, *7*, 513;

[4] B. Acebedo, M. C. Morant-Miñana, E. Gonzalo, I. Ruiz de Larramendi, A. Villaverde, J. Rikarte, L. Fallarino, *Adv. Energy Mater.* **2023**, *13*, 2203744.

[5] a) Y. He, X. Ren, Y. Xu, M. H. Engelhard, X. Li, J. Xiao, J. Liu, J.-G. Zhang, W. Xu, C. Wang, *Nat. Nanotechnol.* **2019**, *14*, 1042; b) W. Liu, D. Lin, A. Pei, Y. Cui, *J. Am. Chem. Soc.* **2016**, *138*, 15443.

[6] a) A. Kushima, K. P. So, C. Su, P. Bai, N. Kuriyama, T. Maebashi, Y. Fujiwara, M. Z. Bazant, J. Li, *Nano Energy* **2017**, *32*, 271; b) C.-J. Ko, C.-H. Chen, K.-C. Chen, *J. Power Sources* **2023**, *563*, 232779.

[7] J. B. Goodenough, Y. Kim, *Chem. Mater.* **2010**, *22*, 587.

[8] a) P. Bai, J. Guo, M. Wang, A. Kushima, L. Su, J. Li, F. R. Brushett, M. Z. Bazant, *Joule* **2018**, *2*, 2434; b) A. Jana, R. E. García, *Nano Energy* **2017**, *41*, 552.

[9] C. Fang, J. Li, M. Zhang, Y. Zhang, F. Yang, J. Z. Lee, M.-H. Lee, J. Alvarado, M. A. Schroeder, Y. Yang, *Nat. Commun.* **2019**, *572*, 511.

[10] a) J. Qian, W. A. Henderson, W. Xu, P. Bhattacharya, M. Engelhard, O. Borodin, J.-G. Zhang, *Nat. Commun.* **2015**, *6*, 6362; b) X.-B. Cheng, R. Zhang, C.-Z. Zhao, Q. Zhang, *Chem. Rev.* **2017**, *117*, 10403; c) J. Wang, T. Bai, Y. Liang, L. Xie, H. Zhang, Z. Zeng, S. Fang, D. Gao, W. Wu, Z. Hu, J. Lu, J. Zhang, L. Ci, D. Li, *ACS Nano* **2025**, *19*, 11284.

[11] a) R. Wang, W. Cui, F. Chu, F. Wu, *J. Energy Chem.* **2020**, *48*, 145; b) J.-M. Tarascon, M. Armand, *Nature* **2001**, *414*, 359; c) X. Zhang, Y. Yang, Z. Zhou, *Chem. Soc. Rev.* **2020**, *49*, 3040; d) A. Patil, V. Patil, D. W. Shin, J.-W. Choi, D.-S. Paik, S.-J. Yoon, *Mater. Res. Bull.* **2008**, *43*, 1913; e) B. Horstmann, J. Shi, R. Amine, M. Werres, X. He, H. Jia, F. Hausen, I. Cekic-Laskovic, S. Wiemers-Meyer, J. Lopez, *Energy Environ. Sci.* **2021**, *14*, 5289.

[12] a) Y. Liu, J. Sun, X. Hu, Y. Li, H. Du, K. Wang, Z. Du, X. Gong, W. Ai, W. Huang, *Nano Energy* **2022**, *94*, 106883; b) S. Kim, M. Lee, S. Oh, W.-H. Ryu, *Chem. Eng. J.* **2023**, *474*, 145447; c) Y. Yuan, F. Wu, Y. Bai, Y. Li, G. Chen, Z. Wang, C. Wu, *Energy Storage Mater.* **2019**, *16*, 411; d) C. Zhang, T. Jin, G. Cheng, S. Yuan, Z. Sun, N.-W. Li, L. Yu, S. Ding, *J. Mater. Chem. A* **2021**, *9*, 13388; e) X. Liang, Q. Pang, I. R. Kochetkov, M. S. Sempere, H. Huang, X. Sun, L. F. Nazar, *Nat. Energy* **2017**, *2*, 1; f) N. W. Li, Y. X. Yin, C. P. Yang, Y. G. Guo, *Adv. Mater.* **2016**, *28*, 1853; g) H. Liu, X. Yue, X. Xing, Q. Yan, J. Huang, V. Petrova, H. Zhou, P. Liu, *Energy Storage Mater.* **2019**, *16*, 505; h) C.-P. Yang, Y.-X. Yin, S.-F. Zhang, N.-W. Li, Y.-G. Guo, *Nat. Commun.* **2015**, *6*, 8058; i) Y. Liu, D. Lin, Z. Liang, J. Zhao, K. Yan, Y. Cui, *Nat. Commun.* **2016**, *7*, 10992; j) S. Zhang, S. Xiao, D. Li, J. Liao, F. Ji, H. Liu, L. J. E. S. M. Ci, *Energy Storage Mater.* **2022**, *48*, 172.

[13] a) J.-S. Lee, K. Shin, S.-Y. Jun, S. Kim, W.-H. Ryu, *Chem. Eng. J.* **2023**, *458*, 141383; b) D. Wu, J. He, J. Liu, M. Wu, S. Qi, H. Wang, J. Huang, F. Li, D. Tang, J. Ma, *Adv. Energy Mater.* **2022**, *12*, 2200337; c) Q. Wang, C. Yang, J. Yang, K. Wu, C. Hu, J. Lu, W. Liu, X. Sun, J. Qiu, H. Zhou, *Adv. Mater.* **2019**, *31*, 1903248.

[14] Q. Liu, L. Wang, *Adv. Energy Mater.* **2023**, *13*, 2301742.

[15] a) Z. Piao, P. Xiao, R. Luo, J. Ma, R. Gao, C. Li, J. Tan, K. Yu, G. Zhou, H. M. Cheng, *Adv. Mater.* **2022**, *34*, 2108400; b) Y. Yin, Y. Yang, D. Cheng, M. Mayer, J. Holoubek, W. Li, G. Raghavendran, A. Liu, B. Lu, D. M. Davies, *Nat. Energy* **2022**, *7*, 548.

[16] Y. Hu, Z. Li, Z. Wang, X. Wang, W. Chen, J. Wang, W. Zhong, R. Ma, *Adv. Sci.* **2023**, *10*, 2206995.

[17] J.-i. Yamaki, S.-i. Tobishima, K. Hayashi, K. Saito, Y. Nemoto, M. Arakawa, *J. Power Sources* **1998**, *74*, 219.

[18] S. Kim, G. Park, S. J. Lee, S. Seo, K. Ryu, C. H. Kim, J. W. Choi, *Adv. Mater.* **2023**, *35*, 2206625.

[19] J. Becherer, D. Kramer, R. Mönig, *J. Mater. Chem. A* **2022**, *10*, 5530.

[20] a) C. Yan, X. B. Cheng, Y. Tian, X. Chen, X. Q. Zhang, W. J. Li, J. Q. Huang, Q. Zhang, *Adv. Mater.* **2018**, *30*, 1707629; b) Y. Liang, W. Wu, D. Li, H. Wu, C. Gao, Z. Chen, L. Ci, J. Zhang, *Adv. Energy Mater.* **2022**, *12*, 2202493.

[21] a) M. Baek, J. Kim, K. Jeong, S. Yang, H. Kim, J. Lee, M. Kim, K. J. Kim, J. W. Choi, *Nat. Commun.* **2023**, *14*, 1296; b) S. Park, R. Chaudhary, S. A. Han, H. Qutaish, J. Moon, M.-S. Park, J. H. Kim, *Energy Materials* **2023**, *3*, 300005.

ADVANCED
SCIENCE NEWS

www.advancedsciencenews.com

NANO · MICRO

small

www.small-journal.com

[22] S. Park, S. Kim, J.-A. Lee, M. Ue, N.-S. Choi, *Chem. Sci.* **2023**, *14*, 9996.
[23] Q. Zhao, Y. Deng, N. W. Utomo, J. Zheng, P. Biswal, J. Yin, L. A. Archer, *Nat. Commun.* **2021**, *12*, 6034.
[24] H. S. Magar, R. Y. Hassan, A. Mulchandani, *Sensors* **2021**, *21*, 6578.
[25] Z. Ogumi, *Electrochemistry* **2010**, *78*, 319.
[26] a) C. Cui, R. Zhang, C. Fu, B. Xie, C. Du, J. Wang, Y. Gao, G. Yin, P. Zuo, *ACS Appl. Mater. Interfaces* **2021**, *13*, 28252; b) H. Yang, L. Yin, H. Shi, K. He, H.-M. Cheng, F. Li, *Chem. Commun.* **2019**, *55*, 13211; c) A. C. Kozen, C.-F. Lin, O. Zhao, S. B. Lee, G. W. Rubloff, M. Noked, *Chem. Mater.* **2017**, *29*, 6298; d) S. Guo, L. Wang, Y. Jin, N. Piao, Z. Chen, G. Tian, J. Li, C. Zhao, X. He, *Nano Converg.* **2020**, *7*, 21; e) W.

Zhang, H. L. Zhuang, L. Fan, L. Gao, Y. Lu, *Sci. Adv.* **2018**, *4*, aar4410; f) H. Wang, J. He, J. Liu, S. Qi, M. Wu, J. Wen, Y. Chen, Y. Feng, J. Ma, *Adv. Funct. Mater.* **2021**, *31*, 2002578; g) S. Y. Jun, K. Shin, J. S. Lee, S. Kim, J. Chun, W. H. Ryu, *Adv. Sci.* **2023**, *10*, 2301426.
[27] P. Hohenberg, W. Kohn, *Phys. Rev.* **1964**, *136*, B864.
[28] a) G. Kresse, D. Joubert, *Phys. Rev. B* **1999**, *59*, 1758; b) G. Kresse, J. Furthmüller, *Phys. Rev. B* **1996**, *54*, 11169.
[29] J. P. Perdew, K. Burke, M. Ernzerhof, *Phys. Rev. Lett.* **1996**, *77*, 3865.
[30] J. M. Zhang, F. Ma, K. W. Xu, *Surf. Interface Anal.* **2003**, *35*, 662.
[31] M. Yu, D. R. Trinkle, *J. Chem. Phys.* **2011**, *134*, 064111.